

Sensitive solution-processed visible-wavelength photodetectors

GERASIMOS KONSTANTATOS, JASON CLIFFORD, LARISSA LEVINA AND EDWARD H. SARGENT*

Department of Electrical and Computer Engineering, University of Toronto, 10 King's College Road, Toronto, Ontario M5S 3G4, Canada

*e-mail: ted.sargent@utoronto.ca

Published online: 3 September 2007; doi:10.1038/nphoton.2007.147

One billion image sensors worldwide render optical images as digital photographs in video cameras, still cameras and camera phones. These silicon-based sensors monolithically integrate photodetection with electronic readout. However, silicon photodiodes rely on a smaller bandgap than that required for visible detection; this degrades visible-wavelength sensitivity and produces unwanted infrared sensitivity. Thin-film top-surface visible photodetectors have therefore been investigated based on amorphous¹, organic² and colloidal quantum-dot³ semiconductors. However, none of these devices has exhibited visible sensitivity approaching that of silicon. Here we report a sensitive solution-processed photodetector that, across the entire visible spectrum, exhibits D^* (normalized detectivity) greater than 5×10^{12} Jones (a unit of detectivity equivalent to $\text{cm Hz}^{1/2} \text{W}^{-1}$). A photoconductive gain of >100 has been measured, facilitating high-fidelity electronic readout, and the linear dynamic range is greater than 60 dB, as required for high-contrast applications. These photodetectors are also compatible with flexible organic-based electronics.

Silicon serves two distinct functions in image sensors. First, silicon photodiodes convert optical signals into electrical signals by means of optical absorption followed by charge separation across a p-n junction. These photodiodes can have high quantum efficiency—approaching 100%—and low noise. As a result, silicon photodiodes are extremely sensitive, providing normalized detectivities typically around 4×10^{12} Jones. Second, silicon transistors enable electronic functions such as photodetector readout, amplification, multiplexing of the output of two-dimensional arrays of pixels into a single time-domain stream, analog-to-digital conversion and digital signal processing.

The monolithic integration of photodetector and readout electronics in a single silicon die simplifies fabrication and scale-up of manufacturing, and thus minimizes cost. Alternatives to monolithic integration, such as hybrid packaging solutions involving bump-bonding a photodetector array to a silicon readout circuit, produce large pixels and thus large chips, as well as lower manufacturing yields and dramatically increased cost compared with monolithically integrated image sensor integrated circuits.

Monolithic integration of photodetectors and electronics does not fundamentally necessitate implementing both functions in crystalline silicon. Complementary metal-oxide semiconductor (CMOS) integration of electronics and optoelectronics in fact reduces the fill factor of CMOS cameras to 30% owing to the coexistence of the electronic transistors and the optically active element on the same chip. Charge-coupled devices (CCDs) on the other hand provide a 100% fill factor at a cost of having two

distinct chips to perform the optical signal acquisition and digital signal processing. Thin-film processes such as spin-coating, evaporation and chemical vapour deposition are therefore widely used to integrate top-surface thin-film photodetectors with the underlying crystalline silicon substrate. The promising amorphous silicon photodetectors suffer from long-lived traps with lifetimes in the hundreds of seconds⁴, and at high intensities exhibit material instabilities⁵. Organic photodetectors² also offer CMOS compatibility, but have yet to demonstrate high sensitivity. Solution-processed semiconductor quantum-dot photodetectors⁶ have demonstrated high sensitivity, but so far only at infrared wavelengths.

Thin-film top-surface photodetectors are also expected to find numerous applications in flexible electronics, delivering low cost, light weight and flexibility. Recent progress in the development and integration of organic transistors⁷ has led to the demonstration of a number of large-area, flexible, low-cost and portable sensors^{8,9}. A flexible optical scanner has been demonstrated based on organic photodetectors, but without any sensitivity characterization reported. The proposed colloidal nanocrystals approach combines solution processibility and high performance for applications in flexible technology.

Any candidate thin-film photodetector must meet several demanding performance requirements simultaneously.

Sensitivity. A top-surface visible-wavelength photodetector for visible imaging must at least match the sensitivity of silicon. One measure of sensitivity is the noise-equivalent power (NEP), the minimum incident optical power that a device can distinguish from noise. However, noise current in a photodetector does not scale linearly with area, so a quantity known as the normalized detectivity D^* , with units of Jones, is defined. D^* is equal to the square root of the optically active area of the detector divided by its NEP. D^* enables comparison between photodetectors of different areas.

Gain. Conventional silicon photodiodes provide up to one electron's worth of current per incident photon. Under low-light conditions, and especially in small pixels, this necessitates the use of extremely low-noise electronic amplifying circuits. Ideally, a photodetector would provide built-in gain, allowing for multiple carriers to be produced by the absorption of a single photon, thus lessening demands on readout circuitry. For example, in photoconductive photodetectors, the creation of an electron–hole pair on absorption of a photon results in an increase in conductivity that persists for the excited carrier lifetime.

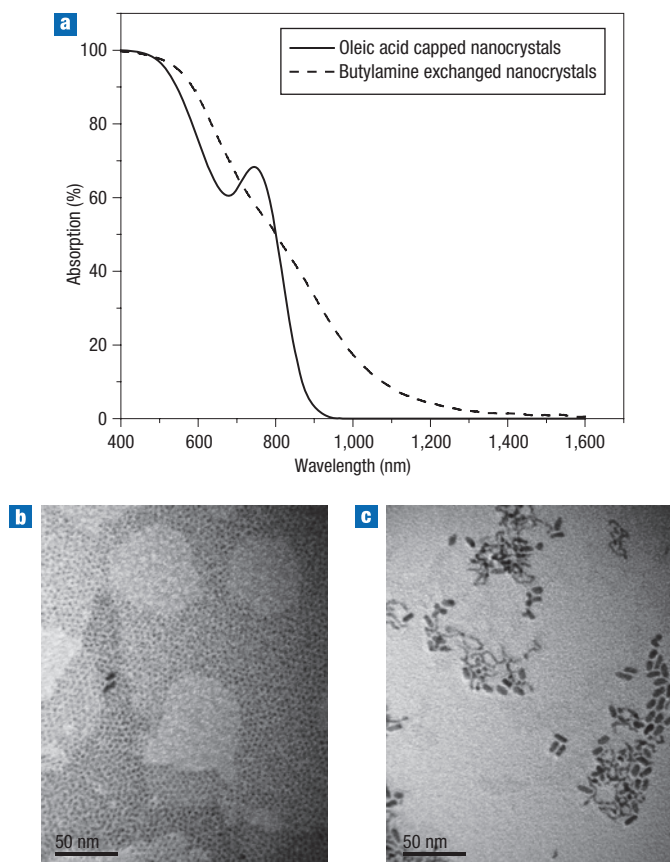


Figure 1 Absorption and transmission electron microscopy (TEM) graphs of small PbS nanocrystals. **a**, Absorption of a solution of as-synthesized oleic-acid-capped nanocrystals and of a solution of the nanocrystals after butylamine ligand exchange. The extended absorption into the infrared is due to loss of high confinement followed by the formation of nanorods. **b**, TEM image of oleic-acid-capped nanocrystals shows the synthesis of small nanocrystals of diameter ~ 3 nm. **c**, After ligand exchange the nanocrystals conglomerate to form nanorods. The scale bar on the bottom left of each TEM graph corresponds to 50 nm.

Tunability. The use of a material system other than silicon opens the possibility of selecting the semiconductor bandgap according to the needs of the application. For visible imaging, the optimal bandgap sensor material would absorb only visible light, obviating the need for an infrared cutoff filter and, by maximizing the bandgap, minimizing generation recombination noise. A tunable materials system also enables a stacked pixel architecture, in which a large-bandgap photodetector senses, and also filters out, higher-energy light, passing only the longer-wavelength light to the independently read pixel elements beneath. Such architectures offer increased low-light sensitivity compared with (lossy) absorbent colour filter arrays used today.

Dynamic range. The ratio of full-well capacity of today's CMOS image sensors to the number of dark electrons limits dynamic range to about three orders of magnitude in intensity (conventionally expressed as 60 dB in imaging). A candidate photodetection device should, at a minimum, provide at least this much dynamic range. Better yet would be a photodetector that, by virtue of its bias-tunable gain, would allow controlled signal compression for dynamic-range enhancement.

A simple, solution-processed route to ultrasensitive ($D^* \sim 1 \times 10^{13}$ Jones) photodetectors has recently been reported⁶. PbS colloidal quantum dots were synthesized, their organic capping ligands exchanged in solution, thin-film photodetectors formed by spin-coating, and a simple solvent developing step used to enhance conductivity and create trap states, resulting in photoconductive gains exceeding 100. However, the reported devices used an infrared bandgap, and the visible-wavelength responsivity and dynamic range were not characterized. Here, we report the simultaneous attainment of sensitivity, gain, tunability and wide dynamic range in a visible-wavelength-sensitive spin-cast photodetector.

As bulk PbS has a bandgap of 0.4 eV, it was necessary to increase dramatically the degree of quantum confinement in these materials to make a visible-only colloidal quantum-dot photoconductive detector. We modified the synthetic procedures of previous reports¹⁰ to synthesize quantum dots with an absorption onset below 800 nm (see Methods). Figure 1a illustrates the absorption spectrum of the resultant quantum dots. As seen in Fig. 1b, the nanoparticles, which have diameters of 3 nm, exhibit faceting. As synthesized, these nanocrystals were stabilized with oleic acid, a configuration expected and observed to impede carrier transport owing to the oleate ligand's long insulating chain. We had previously found that substituting with shorter ligands, such as butylamine, resulted in a dramatic increase in conductivity. In the case of larger nanoparticles of 4–6 nm diameter, monodispersity and excitonic features were preserved after ligand exchange in the solution phase, but for smaller nanocrystals, the procedure led, instead, to the formation of nanorods (Fig. 1c) as previously seen for PbSe nanoparticles¹¹. More problematically, there was loss of an abrupt absorption onset (dashed curve, Fig. 1a) resulting from irreversible aggregation.

We sought an approach that would preserve a sharp, short-wavelength absorption onset. We hypothesized that ligand exchange in the solid state, performed once thin films had already been formed, would limit the number of nanocrystal reattachment sites and markedly improve conductivity without remarkably altering quantum-confined energy levels. PbS nanocrystals dispersed in toluene were spin-coated onto glass substrates with gold interdigitated electrodes with a 5- μ m spacing (see Supplementary Information, Material 1) to form a solid-state film with thickness 360 nm. The optically active area of the detector was then determined by the interelectrode distance (5 μ m) and the electrode length (3 mm). The film was then treated in a mixture of 20% butylamine in acetonitrile over two days. Following this solid-phase ligand exchange, the film exhibited conductivity with dark current density 600 μ A cm⁻² at an applied field of 20 V μ m⁻¹ (see Supplementary Information, Material 2), where the current density was calculated by assuming a cross-section of 360 nm \times 3 mm. Untreated samples or samples treated with acetonitrile alone did not exhibit measurable conductivity.

We characterized the devices for dark current, responsivity and noise current as described in detail in the Methods. We present in Fig. 2 the optoelectronic performance of the photodetectors. Figure 2a shows spectral responsivity and normalized detectivity. The photoconductive gain reaches a maximum of ~ 113 A W⁻¹ at 15 Hz at a wavelength 400 nm. The quantum-dot photodetector has an increasing responsivity at shorter wavelengths and optimal response in the visible part of the spectrum. The electric field to achieve this gain was 20 V μ m⁻¹, which for the 5- μ m interelectrode gap translated to an applied bias of 100 V. A 500-nm-thick film would require 10 V to achieve the same field and gain.

The responsivity of these devices arises from the product of absorbance and photoconductive gain. We measured the

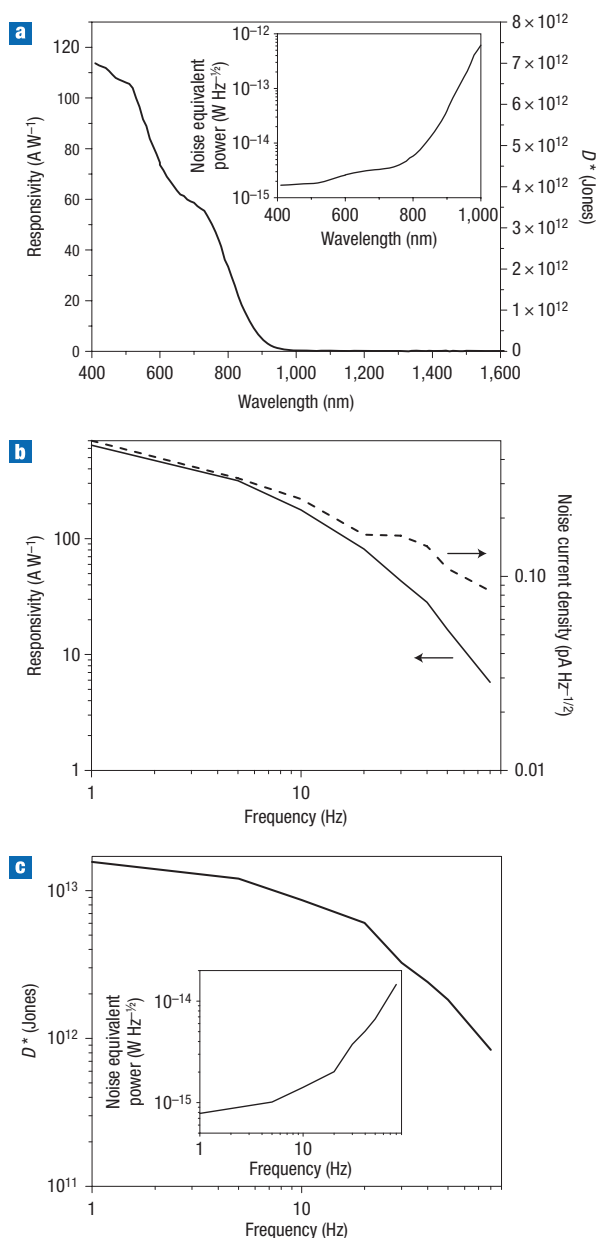


Figure 2 Performance of the PbS small nanocrystal photodetector.

a, Spectral responsivity and normalized detectivity D^* taken at 15 Hz modulation frequency. The inset shows the NEP of the 0.0015-mm² detector in the visible range for a modulation frequency of 15 frames per second. **b**, Responsivity and noise current density (left and right vertical axis respectively as indicated by the arrows) versus modulation frequency. **c**, The detector exhibits $D^* \sim 10^{13}$ Jones for modulation frequency up to 5 Hz, whereas it has D^* greater than 10^{12} Jones up to 70 Hz at a wavelength of 400 nm. The inset shows the resultant NEP of the detector at 400 nm with active area 0.0015 mm² as a function of modulation frequency.

absorbance of these devices in the visible to be 0.2. Photoconductive gain arises from sensitization of PbS with electron trap states that elongate the carrier lifetime of the holes⁶: gain is equal to the ratio of carrier lifetime to transit time. Lifetime estimated from the 3-dB bandwidth of the device is 8 Hz, which corresponds to an effective lifetime of 125 ms. A

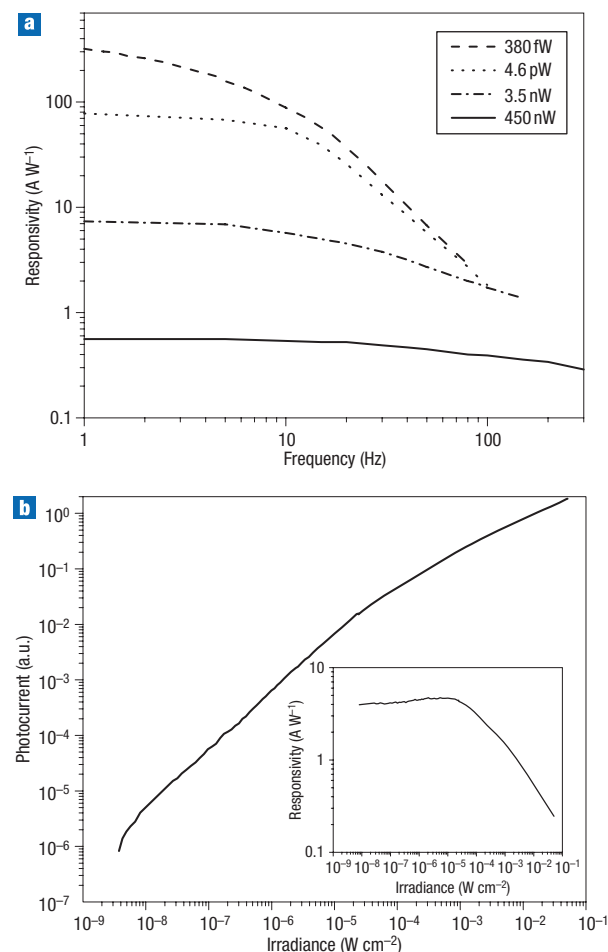


Figure 3 Effects of the trap states on photodetector performance.

a, Responsivity versus modulation frequency at various illumination levels measured at an optical wavelength of 632 nm. The long-lived trap states dominate at low optical powers to provide high photoconductive gain. As higher power impinges on the detector, the effective traps are filled, leading to a decrease of the photoconductive gain and increase of the 3-dB bandwidth. The 3-dB bandwidth increases from 8 Hz at low power to over 300 Hz at high optical power. This phenomenon could provide the detector with a self-limiting gain mechanism to avoid electronic saturation at high power levels.

b, The photocurrent versus optical illumination reveals a dynamic range of 7.5 orders of magnitude (conventionally expressed as 150 dB). The inset shows responsivity as a function of optical intensity. The responsivity drops beyond 2×10^{-5} W cm⁻² owing to the filling of the high-gain trap states to enable the self-limiting mechanism of gain. This measurement was taken with light at 830 nm.

value of gain measured in the hundreds is consistent with a transit time in the hundreds of microseconds, in turn consistent with a mobility of the order of 10^{-5} cm² V⁻¹ s⁻¹, determined experimentally using time-of-flight measurements.

The measured noise-current spectrum is shown in the inset of Fig. 2b. At low frequencies, the noise current density closely follows the responsivity curve, suggesting that the carrier traps responsible for high gain also contribute to noise, but at higher frequencies, white noise dominates. The Johnson noise of the detector is estimated from $(4kTB/R)^{1/2}$ to be ~ 0.9 fA Hz^{-1/2}, whereas the shot noise limit $(2qI_dB)^{1/2}$ is found to be 0.04 pA Hz^{-1/2}, where k is the Boltzmann constant, T is temperature, R is the resistance

of the detector in the dark, B is the noise bandwidth, q is the electron charge and I_d is the dark current. Our detector approaches the shot noise limit to within 3 dB at 80 Hz. The resultant D^* is plotted as a function of frequency in Fig. 2c (the inset also shows NEP versus modulation frequency). At low frequencies (<5 Hz) the detector exhibits $D^* \sim 10^{13}$ Jones. This photoconductive device, although it exhibits a higher dark current than sensitive photodiodes, achieves excellent sensitivity by virtue of its low noise current. The photoconductive photodetector's bandwidth is low owing to long-lived sensitizing electron traps that provide gain; however, the sensitivity and bandwidth are appropriate for imaging applications at 15 frames per second.

We sought to investigate further the trap states responsible for photoconductive gain. In Fig. 3a, we present the measured responsivity as a function of modulation frequency for a number of different optical power levels incident on the device. The responsivity of the detector decreases as the optical power is increased. We attribute this to filling of the lowest-lying, longest-lived trap states that provide the highest photoconductive gain at low intensities. This is confirmed by the fact that, at high intensities, the 3-dB bandwidth extends to higher electrical frequencies.

To characterize the impact of high-gain trap-state filling on the dynamic range of the solution-processed detector, we measured the dependence of photocurrent on optical intensity at a modulation frequency of 30 Hz. We observed a monotonic, though at high intensities sublinear, dependence of photocurrent on intensity over more than 7.5 orders of magnitude in incident intensity corresponding to over 150 dB of intensity dynamic range (Fig. 3b). The linear part of the curve extends for over 3 orders of magnitude, corresponding to 60 dB of intensity linear dynamic range, which is what is typically required for most imaging applications. At higher optical intensities, however, the detector exhibits an inherent sublinear transformation of the optical signal to electrical output desired for increased intrasene dynamic range¹² (the ability to detect very bright and very dim parts of the same image). The inset of Fig. 3b shows the onset of responsivity decrease owing to the filling of the high-gain trap states at higher intensities that is responsible for gain compression.

METHODS

PBS NANOCRYSTAL SYNTHESIS

A typical synthesis of PbS nanocrystals with an excitonic peak between 700 nm and 800 nm involved injection of 2.0 mmol bis(trimethylsilyl)sulphide into a reaction flask containing 4.0 mmol lead oxide (0.9 g), 9.5 mmol oleic acid (2.67 g) and 18.8 mmol octadecene (4.73 g) at 80 °C. After the injection, the reaction was quenched by moving the flask to an ice-water bath. The synthesis was carried out under inert conditions using a Schlenk line. The final PbS oleate-capped nanocrystals were isolated from any remaining starting materials and side products by precipitating with acetone. The precipitate was then re-dissolved in toluene and precipitated again with acetone. The final nanocrystals were re-dispersed in toluene for device fabrication.

RESPONSIVITY MEASUREMENT

The responsivity was measured by two different methods. In the first, a 2-mm-radius beam from a 975-nm laser was incident, first through a series of optical attenuators of known transmittance, and through the glass substrate, onto the device from the backside. On the top surface, infrared-opaque interdigitated gold electrodes were separated by 5 μm over a 3-mm path length. The optical power incident on the device was obtained by integrating the intensity profile of the laser over the unobstructed area of the device. Current–voltage characteristics were acquired using an Agilent 4155 semiconductor parameter analyser. The responsivity at different frequencies was measured by electrical modulation of the laser.

In the second method, bias was applied to the sample connected in series with a 2-M Ω load resistor. Illumination was provided by a white light source (ScienceTech Inc. TH-2) dispersed by a Triax 320 monochromator and mechanically chopped at the frequency of interest. Optical filters were used to prevent grating overtones from illuminating the sample. The voltage across the load resistor was measured using a Stanford Research Systems SR830 lock-in amplifier. The intensity transmitted through the monochromator at each wavelength was measured separately using calibrated Ophir PD-300 Si and Ge photodetectors to cover the range 400–1,600 nm. The optical power impinging on the active area of the detector was calculated by dividing the active area of the device by the collimated beam area and multiplying by the total power measured with the calibrated detectors. The photocurrent at each wavelength was subsequently scaled according to this system calibration.

The set-up described in the previous paragraph allowed measurement of spectral responsivity by using a variable attenuator programmed to fix the optical power at each wavelength. The recorded photocurrent versus wavelength yielded the spectral responsivity.

The results of the two aforementioned techniques agreed to within less than 10%.

NOISE MEASUREMENT

Dark current noise in the photodetectors was measured using a Stanford Research SR830 lock-in amplifier. The devices were biased using alkaline batteries, and testing was carried out in an electrically shielded and optically sealed probe station, and on a floating table to minimize vibrational noise. The reported noise current, normalized to the measurement bandwidth, divided by the responsivity under the same measurement conditions, yielded the NEP. The normalized detectivity D^* was obtained as a function of wavelength, applied bias and centre frequency by dividing the square root of the optically active area of the device by the NEP.

DYNAMIC RANGE MEASUREMENT

The same set-up as used in spectral responsivity measurement was used. The wavelength was fixed at 830 nm and a variable attenuator combined with neutral density filters was used to vary the light intensity from pW up to 4 μW . For higher intensities, a semiconductor laser at 830 nm was used to provide optical powers up to 10 mW.

Received 7 February 2007; accepted 11 July 2007; published 3 September 2007.

References

1. Theil, J. A. a-Si:H photodiode technology for advanced CMOS active pixel sensor imagers. *J. Non-Cryst. Solids* **299–302**, 1234–1239 (2002).
2. Peumans, P., Bulovic, V. & Forrest, S. R. Efficient, high-bandwidth organic multilayer photodetectors. *Appl. Phys. Lett.* **76**, 3855–3857 (2000).
3. Oertel, D. C., Bawendi, M. G., Arango, A. C. & Bulovic, V. Photodetectors based on treated CdSe quantum-dot films. *Appl. Phys. Lett.* **87**, 213505–213507 (2005).
4. Vygranenko, Y., Chang, J. H. & Nathan, A. Two-dimensional a-Si: H n-i-p photodiode array for low-level light detection. *IEEE J. Quant. Electron.* **41**, 697–703 (2005).
5. Staebler, D. L. & Wronski, C. R. Reversible conductivity changes in discharge-produced amorphous Si. *Appl. Phys. Lett.* **31**, 292–294 (1977).
6. Konstantatos, G. *et al.* Ultrasensitive solution-cast quantum dot photodetectors. *Nature* **442**, 180–183 (2006).
7. Crone, B. *et al.* Large-scale complementary integrated circuits based on organic transistors. *Nature* **403**, 521–523 (2000).
8. Someya, T. *et al.* A large-area, flexible pressure sensor matrix with organic field-effect transistors for artificial skin applications. *Proc. Natl Acad. Sci. USA* **101**, 9966–9970 (2004).
9. Someya, T. *et al.* Integration of organic FETs with organic photodiodes for a large area, flexible, and lightweight sheet image scanners. *IEEE Trans. Electron. Devices* **52**, 2502–2511 (2005).
10. Hines, M. A. & Scholes, G. D. Colloidal PbS nanocrystals with size-tunable near-infrared emission: observation of post-synthesis self-narrowing of the particle size distribution. *Adv. Mater.* **15**, 1844–1849 (2003).
11. Cho, K. S., Talapin, D. V., Gaschler, W. & Murray, C. B. Designing PbSe nanowires and nanorings through oriented attachment of nanoparticles. *J. Am. Chem. Soc.* **127**, 7140–7147 (2005).
12. Fossum, E. R. CMOS image sensors: Electronic camera-on-a-chip. *IEEE Trans. Electron. Dev.* **44**, 1689–1698 (1997).

Acknowledgements

The authors thank S. Hoogland for assembling part of the experimental set-ups used and D. Holmyard for his help with transmission electron microscopy imaging. Correspondence and requests for materials should be addressed to E.H.S. Supplementary information accompanies this paper on www.nature.com/naturephotonics.

Competing financial interests

The authors declare no competing financial interests.

Reprints and permission information is available online at <http://npg.nature.com/reprintsandpermissions/>